Supporting Information for

Laser Derived Interfacial Confinement Enables Planar Growth of 2D SnS_2 on Graphene for High-Flux Electron/Ion Bridging in Sodium Storage

Xiaosa Xu[#], Fei Xu[#], Xiuhai Zhang, Changzhen Qu, Jinbo Zhang, Yuqian Qiu, Rong Zhuang, and Hongqiang Wang*

State Key Laboratory of Solidification Processing, Centre for Nano Energy Materials, School of Materials Science and Engineering, Northwestern Polytechnical University, Shaanxi Joint Laboratory of Graphene (NPU), Xi'an, 710072, P. R. China.

[#] These authors contributed equally to this work.

*Corresponding author. E-mail: hongqiang.wang@nwpu.edu.cn (Hongqiang Wang)

S1 Theoretical Calculation

DFT calculations were conducted via CASTEP program along with the generalized gradient approximation (GGA) from the Perdew-Burke-Ernzerhof (PBE) defined electronic exchange-correlation interaction. The model systems were optimized based on the (2 × 2 × 1) SnS_2 supercell on (6 × 6 × 1) graphene supercell. The vacuum distance of graphene was set as 15 Å to avoid interactions between neighboring layers. A cutoff energy of 517 eV was set and the Monkhorst-Pack k-point grid was 2×2×1. The convergence conditions for geometry optimization were as below: 1.0×10^{-5} eV/atom for energy, 0.03 eV/Å for force, 0.05 GPa for stress, and 0.001 Å for displacement, respectively. The Bader charge was obtained via analyzing the charge density gained from the VASP.

S2 Supplementary Figures

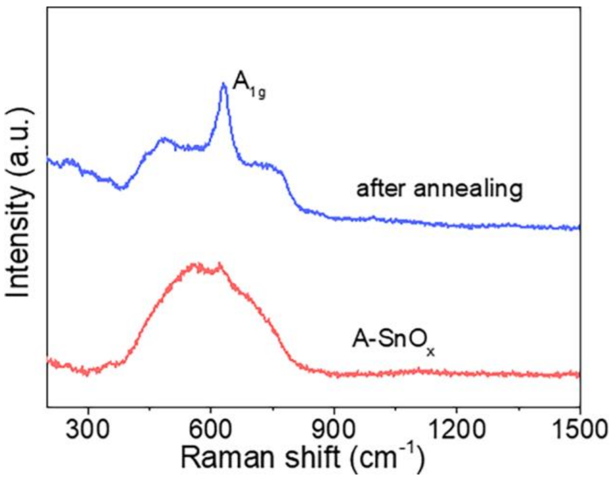

Fig. S1 Raman patterns of A-SnO_x and annealing in nitrogen

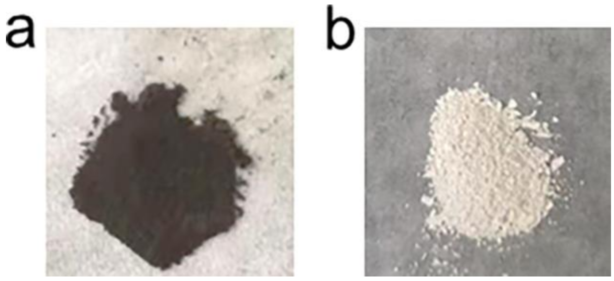

Fig. S2 Photographs of **a** A-SnO_x powder and **b** SnO_2 powder

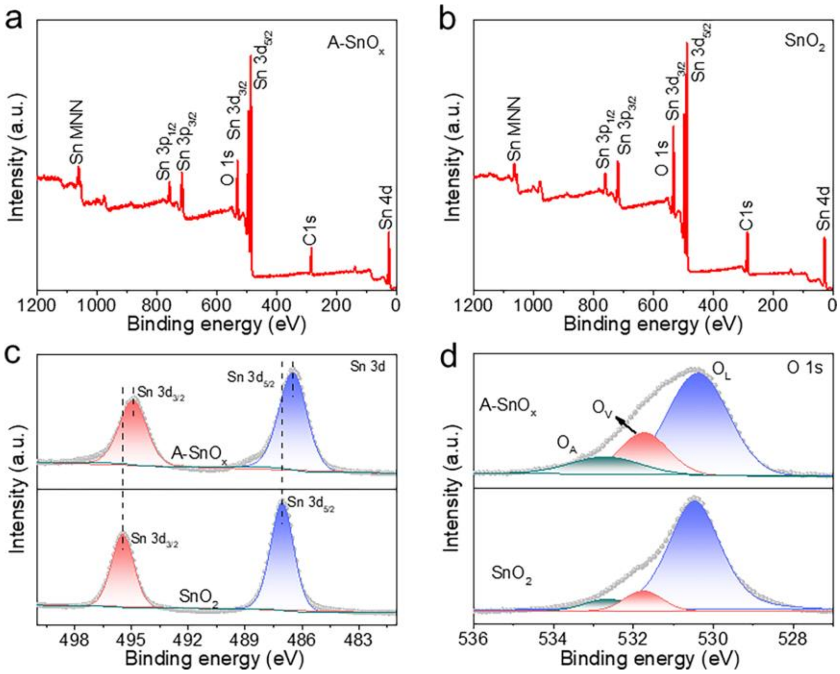

Fig. S3 XPS survey spectra of **a** A-SnO_x and **b** bulk SnO_2. **c** XPS Sn 3d spectra and **d** O 1s spectra of A-SnO_x and bulk SnO_2

As shown in Fig. S3d, the fitted peak area assigned to oxygen vacancies in A-SnO_x is much large than that of bulk SnO_2. Combined with the obvious downshift of Sn $3d_{5/2}$ and $3d_{3/2}$ peaks of A-SnO_x (Fig. S3c), it proves the existence of abundant oxygen vacancies in laser- manufactured A-SnO_x.

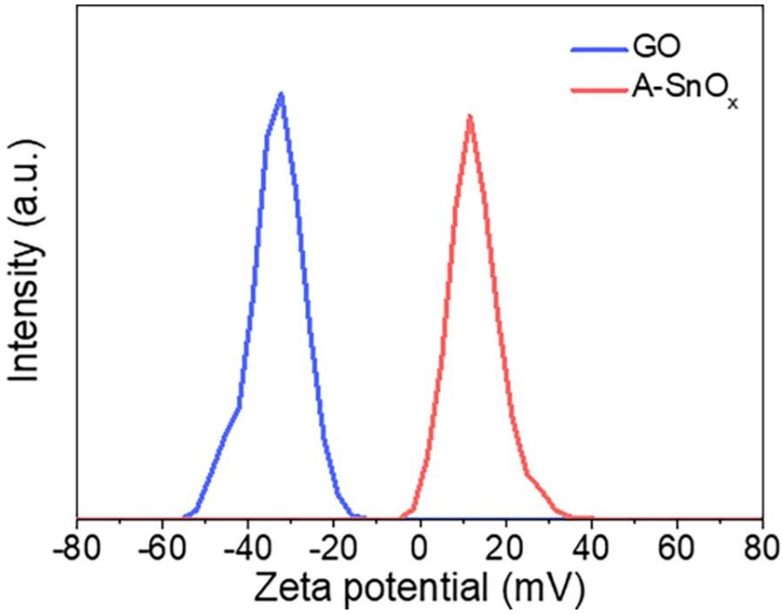

Fig. S4 Zeta potentials of GO and A-SnO$_x$

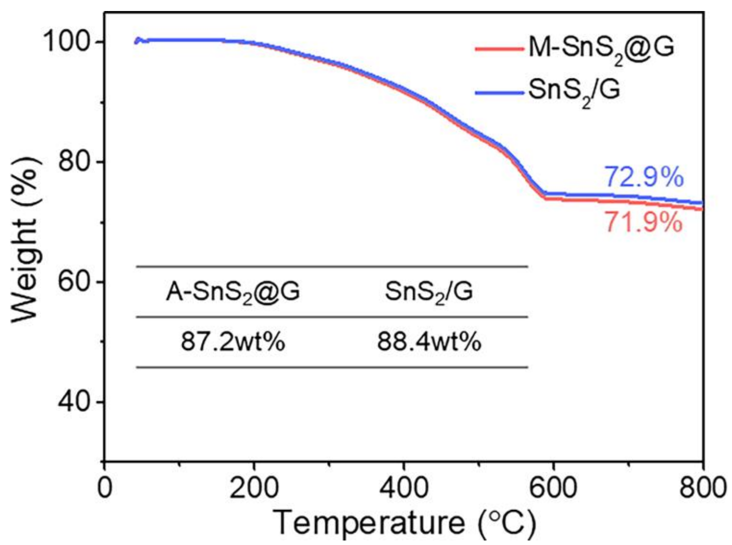

Fig. S5 TGA curves of A-SnS_2@G and SnS_2/G

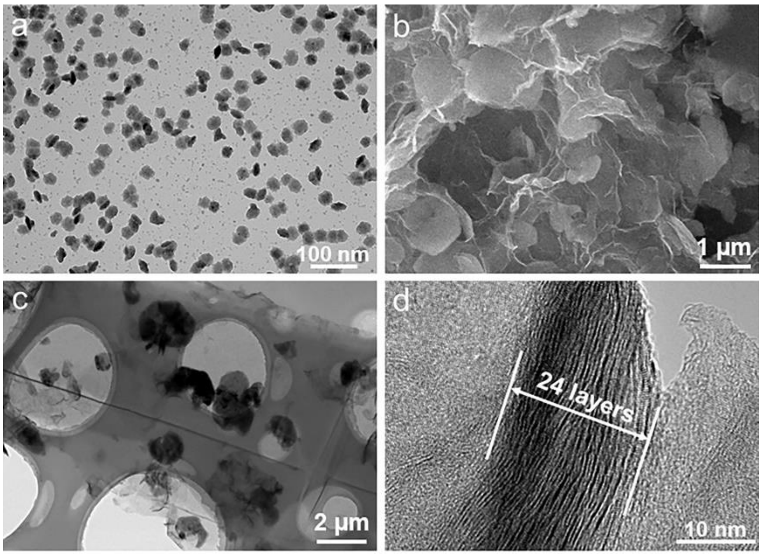

Fig. S6 a TEM image of large A-SnO_x particles (~25 nm). **b** SEM image, **c** TEM image at low magnification, and **d** TEM image at high resolution of A-SnS_2@G with large A-SnO_x particles as seeds

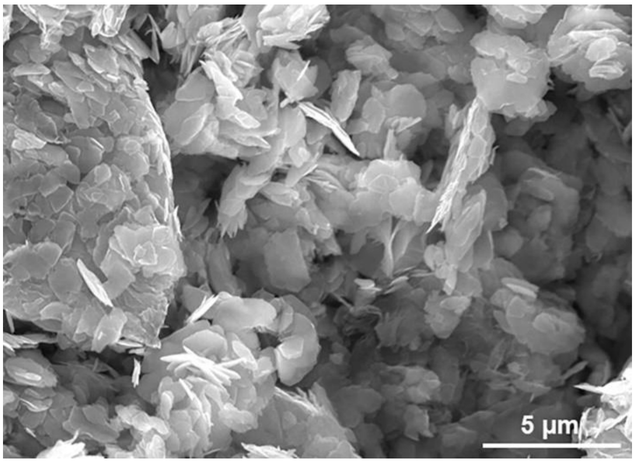

Fig. S7 SEM image of SnS_2

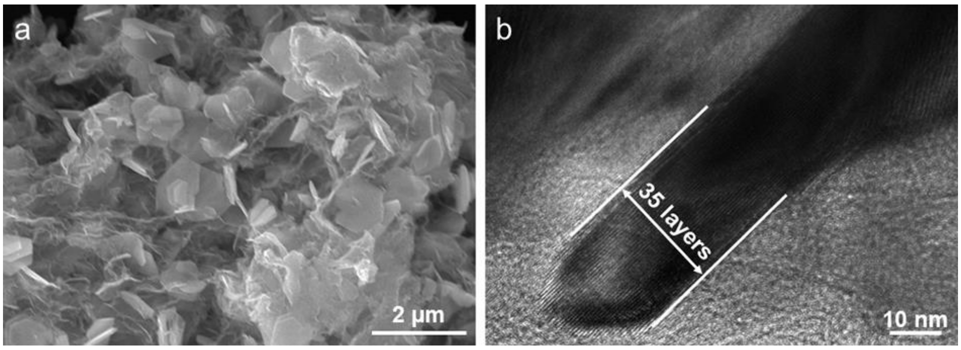

Fig. S8 a SEM and **b** TEM images of SnS_2/G

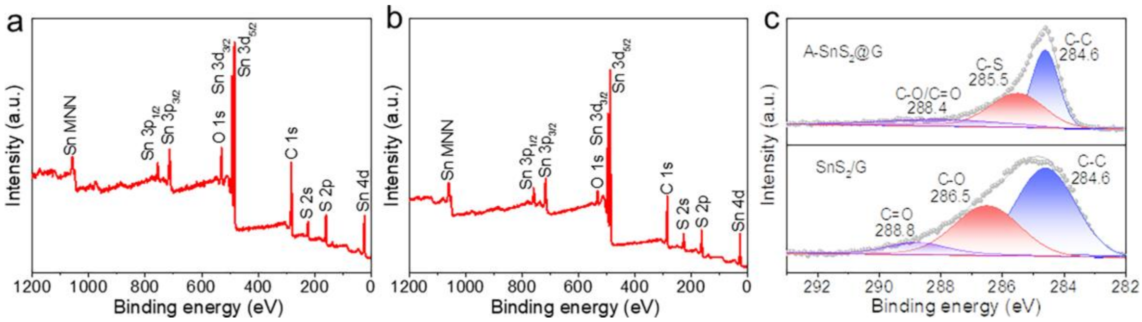

Fig. S9 XPS survey spectra of **a** A-SnS_2@G and **b** SnS_2/G. **c** XPS C 1s spectra of A-SnS_2@G and SnS_2/G

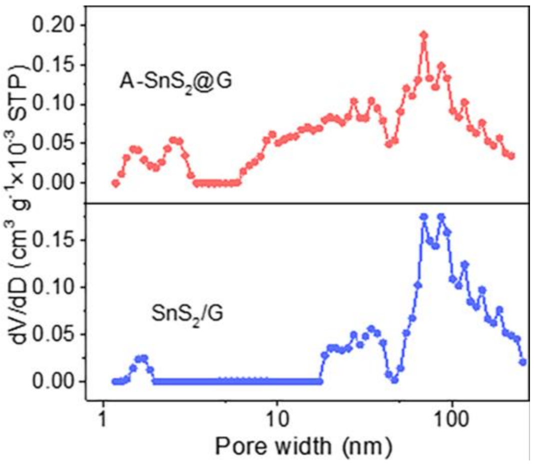

Fig. S10 Pore size distribution curves of A-SnS_2@G and SnS_2/G

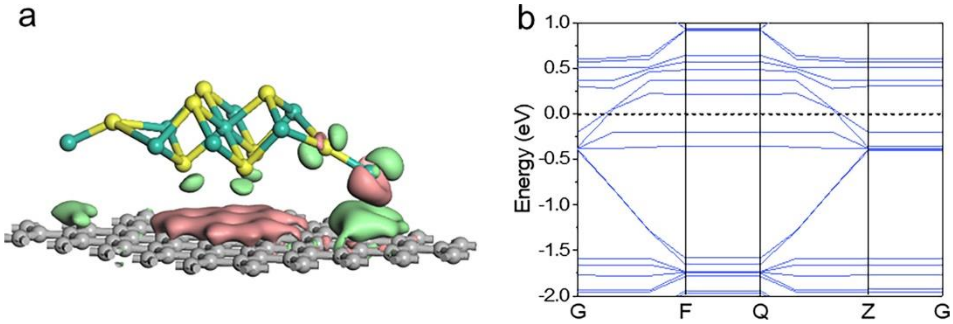

Fig. S11 a Charge density difference and **b** band structure of optimized A-SnS_2@G model (the green/pink cloud represents the accumulation/depletion of electrons)

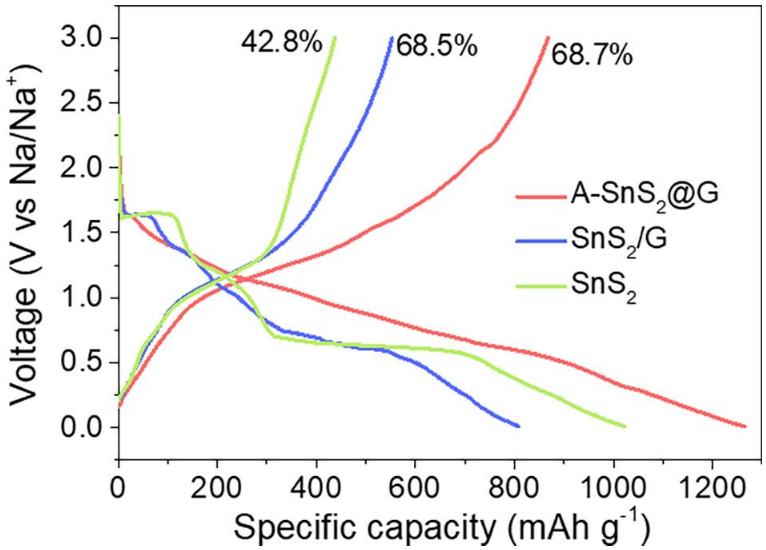

Fig. S12 The initial charge/discharge profile of A-SnS_2@G, SnS_2/G, and SnS_2 electrodes at 0.1 A g^{-1}

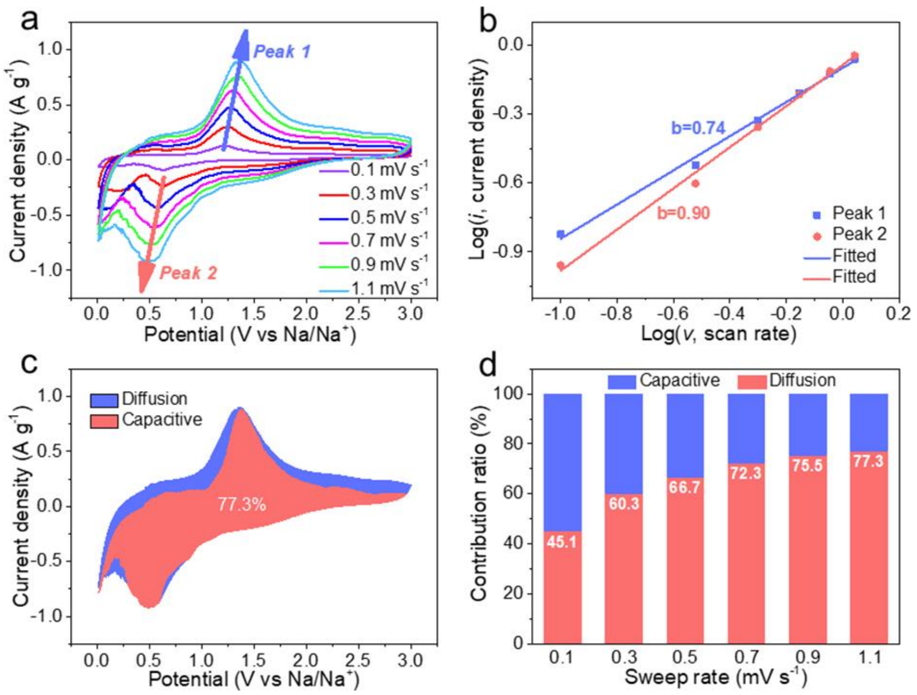

Fig. S13 a CV curves of SnS_2/G electrode at 0.1-1.1 mV s^{-1}. **b** Corresponding log(*i*) versus log(*v*) plots for anodic and cathodic peaks. **c** Capacitive contribution at 1.1 mV s^{-1} for SnS_2/G. **d** Contribution ratio of the capacitive and diffusion-limited capacity at different sweep rates

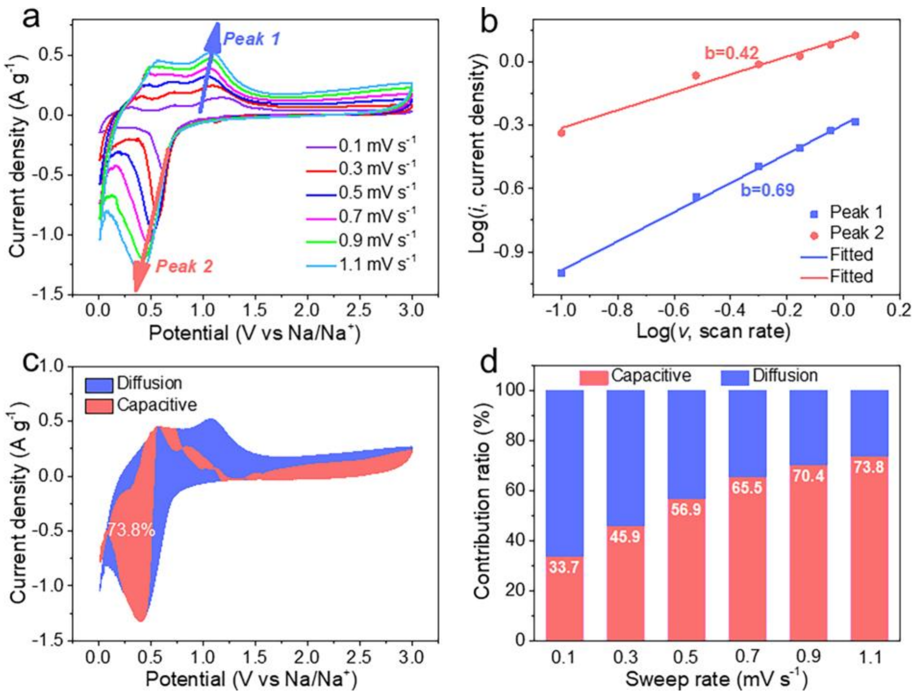

Fig. S14 a CV curves of SnS_2 electrode at 0.1-1.1 mV s^{-1}. **b** Corresponding log(*i*) versus log(*v*) plots for anodic and cathodic peaks. **c** Capacitive contribution at 1.1 mV s^{-1} for SnS_2. **d** Contribution ratio of the capacitive and diffusion-limited capacity at different sweep rates

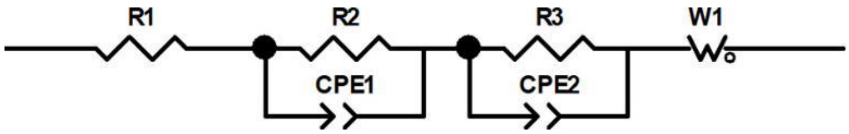

Fig. S15 Corresponding equivalent circuit used to simulate EIS curves

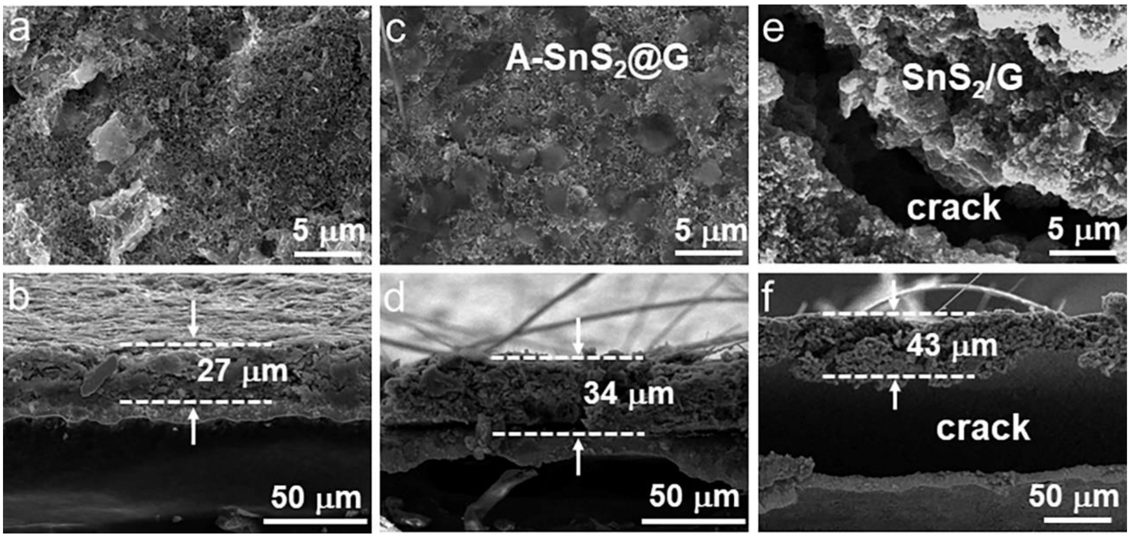

Fig. S16 Top-view and cross-section SEM images of **a, b** fresh A-SnS_2@G electrode, **c, d** A-SnS_2@G electrode after cycling, and **e, f** SnS_2/G electrode after cycling, respectively

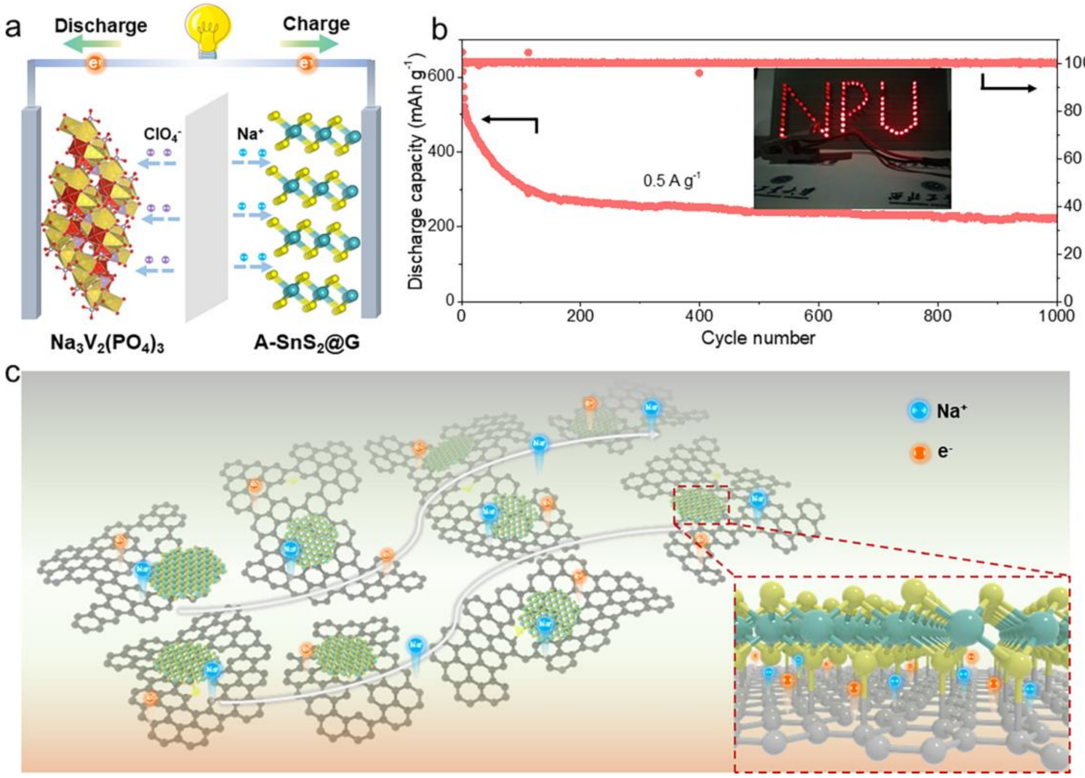

Fig. S17 a Schematic illustration of the full cell configuration coupled with the $Na_3V_2(PO_4)_3$ cathode. **b** Cycling performance of the full cell at 0.5 A g^{-1} (the inset is digital image of LEDs lighted by a full cell). **c** Schematic illustration of interface bridging effect on Na-storage

S3 Supplementary Tables

Table S1 Summary of the pore parameters for A-SnS_2@G and SnS_2/G.

Sample	S_{BET} (m^2 g^{-1})	P_{mic} (%)	P_{mes} (%)	P_{mac} (%)
A-SnS_2@G	53.3	4.9	51	44.1
SnS_2/G	19.6	3.0	18.7	78.3

Micro-, meso- and macropore ratios (P_{mic}, P_{mes} and P_{mac}, respectively) are calculated according to the following equations: $P_{mic} = (V_{mic}/V_{sum}) \times 100\%$, $P_{mes} = (V_{mes}/V_{sum}) \times 100\%$, and $P_{mac} = 100\% - P_{mic} - P_{mes}$, where V_{mic}, V_{mes}, V_{mac} and V_{sum} are the cumulative volume of Micro-, meso-, macro-pore and total pore.

Table S2 The corresponding parameters from the equivalent circuit simulation.

Sample	R1 (Ohm)	R2 (Ohm)	R3 (Ohm)	CPE1 (F)	CPE2 (F)
A-SnS_2@G	5.80	8.81	47.78	8.59E-06	3.51E-05
SnS_2/G	4.06	9.49	131.9	1.04E-05	2.97E-05
SnS_2	7.62	83.21	186.9	1.21E-05	4.87E-05

R_{ct}=R2+R3.

Table S3 Comparison of Na-storage performance of SnS_2@NSG with the reported SnS_2-based anode materials.

Materials	Current density (A g^{-1})								Ref.
	0.1	0.2	0.5	1	2	5	10	20	
SnS_2/NSDC	581.7	548.7	513.7	458.2	407.4	--	--	--	[S1]
3D-GNS/SnS_2	590	500	445	390	265	180	--	--	[S2]
SnS_2@CoS_2-rGO	--	558	552	468	396	--	--	--	[S3]
SnS_2 NC/EDA-RGO	0.46	0.93	1.86	3.71	5.57	7.43	9.3	11.2	[S4]
	630	560	510	435	370	315	280	250	
SnS_2/rGO	649	582	0.4	0.8	1.6	3.2	6.4	12.8	[S5]
			570	550	524	501	452	337	
SnS_2-RGO	670	650	620	575	544	--	--	--	[S6]
SnS_2@C	695.5	--	--	604.1	507.6	304.4	--	--	[S7]
SnS_2@CNSs	709	696	632	576	517	410	--	--	[S8]
SnS_2/NS-CNT	0.11	0.23	0.45	1.14	2.27	3.41	4.54	5.68	[S9]
	738	613	538	463	411	382	360	344	
SnS_2@C	750	668	614	548	438	362	452	337	[S10]
SF-SnS_2@NPC	840	800	0.4	0.8	1.6	3.2	6.4	12.8	[S11]
			735	690	608	530	450	378	
B-SnS_2	--	940	860	780	680	530	400	--	[S12]
P-SnS_2@TiC/C	1293.8	1169.8	943.3	843.7	605.8	476.4	--	--	[S13]
SnS_2/CNTs	690	554	437	368	282	--	--	--	[S14]
A-SnS_2@G	**1081**	**827**	**763**	**718**	**655**	**533**	**410**	**259**	**This work**

Specific capacity: mAh g^{-1}

Supplementary References

[S1] J. Xia, K. Z. Jiang, J. J. Xie, S. H. Guo, L. Liu et al., Tin disulfide embedded in N-, S-doped carbon nanofibers as anode material for sodium-ion batteries. Chem. Eng. J. **359**, 1244-1251 (2019). https://doi.org/10.1016/j.cej.2018.11.053

[S2] Z. Y. Sang, X. Yan, D. Su, H. M. Ji, S. H. Wang et al., A flexible film with SnS_2 nanoparticles chemically anchored on 3D-graphene framework for high areal density and high rate sodium storage. Small **16**(25), 2001265 (2020). https://doi.org/10.1002/smll.202001265

[S3] X. Wang, X. Y. Li, Q. Li, H. S. Li, J. Xu et al., Improved electrochemical performance based on nanostructured SnS_2@CoS_2-rGO composite anode for sodium-ion batteries. Nano-Micro Lett. **10**(3), 46 (2018). https://doi.org/10.1007/s40820-018-0200-x

[S4] Y. Jiang, M. Wei, J. K. Feng, Y. C. Ma, S. L. Xiong, Enhancing the cycling stability of Na-ion batteries by bonding SnS_2 ultrafine nanocrystals on amino-functionalized graphene hybrid nanosheets. Energy Environ. Sci. **9**(4), 1430-1438 (2016). https://doi.org/10.1039/c5ee03262h

[S5] Y. D. Zhang, P. Y. Zhu, L. L. Huang, J. Xie, S. C. Zhang et al., Few-layered SnS_2 on few-layered reduced graphene oxide as Na-ion battery anode with ultralong cycle life and superior rate capability. Adv. Funct. Mater. **25**(3), 481-489 (2015). https://doi.org/10.1002/adfm.201402833

[S6] B. H. Qu, C. Z. Ma, G. Ji, C. H. Xu, J. Xu et al., Layered SnS_2-reduced graphene oxide composite-a high-capacity, high-rate, and long-cycle life sodium-ion battery anode material. Adv. Mater. **26**(23), 3854-3859 (2014). https://doi.org/10.1002/adma.201306314

[S7] S. H. Li, Z. P. Zhao, C. Q. Li, Z. Y. Liu, D. Li, SnS_2@C hollow nanospheres with robust structural stability as high-performance anodes for sodium ion batteries. Nano-Micro Lett. **11**(1), 14 (2019). https://doi.org/10.1007/s40820-019-0243-7

[S8] Y. Liu, X. Y. Yu, Y. J. Fang, X. S. Zhu, J. C. Bao et al., Confining SnS_2 ultrathin nanosheets in hollow carbon nanostructures for efficient capacitive sodium storage. Joule **2**(4), 725-735 (2018). https://doi.org/10.1016/j.joule.2018.01.004

[S9] Z. J. Liu, A. Daali, G. L. Xu, M. H. Zhuang, X. B. Zuo et al., Highly reversible sodiation/desodiation from a carbon-sandwiched SnS_2 nanosheet anode for sodium ion batteries. Nano Lett. **20**(5), 3844-3851 (2020). https://doi.org/10.1021/acs.nanolett.0c00964

[S10] Q. Sun, D. P. Li, L. N. Dai, Z. Liang, L. J. Ci, Structural engineering of SnS_2 encapsulated in carbon nanoboxes for high-performance sodium/potassium-ion batteries anodes. Small **16**(45), 2005023 (2020). https://doi.org/10.1002/smll.202005023

[S11] X. Xu, R. S. Zhao, B. Chen, L. S. Wu, C. J. Zou et al., Progressively exposing active facets of 2D nanosheets toward enhanced pseudocapacitive response and high-rate sodium storage. Adv. Mater. **31**(17), 1900526 (2019). https://doi.org/10.1002/adma.201900526

[S12] D. L. Chao, P. Liang, Z. Chen, L. Y. Bai, H. Shen et al., Pseudocapacitive Na-ion storage boosts high rate and areal capacity of self-branched 2D layered metal chalcogenide nanoarrays. ACS Nano **10**(11), 10211-10219 (2016). https://doi.org/10.1021/acsnano.6b05566

[S13] Y. B. Shen, S. J. Deng, P. Liu, Y. Zhang, Y. H. Li et al., Anchoring SnS_2 on TiC/C backbone to promote sodium ion storage by phosphate ion doping. Small **16**(40), 2004072 (2020). https://doi.org/10.1002/smll.202004072

[S14] L. Zhu, X. X. Yang, Y. H. Xiang, P. Kong, X. W. Wu, Neurons-system-like structured SnS_2/CNTs composite for high-performance sodium-ion battery anode. Rare Metals **40**(6), 1383-1390 (2020). https://doi.org/10.1007/s12598-020-01555-6